OATAO

Open Archive Toulouse Archive Ouverte

Open Archive Toulouse Archive Ouverte (OATAO)

OATAO is an open access repository that collects the work of some Toulouse researchers and makes it freely available over the web where possible.

This is an author's version published in: https://oatao.univ-toulouse.fr/27437

Official URL: https://doi.org/10.2514/1.G005368

To cite this version :

Any correspondence concerning this service should be sent to the repository administrator: tech-oatao@listes-diff.inp-toulouse.fr

Aided Inertial Estimation of Wing Shape

Leandro R. Lustosa,* Ilya Kolmanovsky,† and Carlos E. S. Cesnik‡
University of Michigan, Ann Arbor, Michigan 48109-2140
and
Fabio Vetrano§
Airbus Operations S.A.S., 31060 Toulouse, France

Advanced large-wing-span aircraft result in more structural flexibility and the potential for instability or poor handling qualities. These shortcomings call for stability augmentation systems that entail active structural control. Consequently, the in-flight estimation of wing shape is beneficial for the control of very flexible aircraft. This paper proposes a new methodology for estimating flexible structural states based on extended Kalman filtering by exploiting ideas employed in aided inertial navigation systems. High-bandwidth-rate gyro angular velocities at different wing stations are integrated to provide a short-term standalone inertial shape estimation solution, and additional low-bandwidth aiding sensors are then employed to bound diverging estimation errors. The proposed filter implementation does not require a flight dynamics model of the aircraft, facilitates the often tedious Kalman filtering tuning process, and allows for accurate estimation under large and nonlinear wing deflections. To illustrate the approach, the technique is verified by means of simulations using sighting devices as aiding sensors, and an observability study is conducted. In contrast to previous work in the literature based on stereo vision, a sensor configuration that provides fully observable state estimation is found using only one camera and multiple rate gyros for Kalman filtering update and prediction phases, respectively.

Nomenclature

$D \in \mathbb{R}^{3\times3}$	=	direction cosine matrix
$H \in \mathbb{R}^{3\times3}$	=	angular velocity to Euler angles rate transformation
$H_\theta \in \mathbb{R}^{1\times3}$	=	angular velocity to pitch rate transformation
$H_\phi \in \mathbb{R}^{1\times3}$	=	angular velocity to roll rate transformation
$H_\psi \in \mathbb{R}^{1\times3}$	=	angular velocity to yaw rate transformation
$K \in \mathbb{Z}_+^*$	=	number of cameras
$M \in \mathbb{Z}_+^*$	=	number of rate gyros
$N \in \mathbb{Z}_+^*$	=	number of mode shapes
$P_b \in \mathbb{R}$	=	rigid-body angular velocity (x axis)
$\hat{P}_b \in \mathbb{R}$	=	rigid-body rate gyro output (x axis)
$P_j \in \mathbb{R}$	=	jth station angular velocity (x axis)
$\hat{P}_j \in \mathbb{R}$	=	jth rate gyro output (x axis)
$\boldsymbol{p}^{k/l} \in \mathbb{R}^3$	=	position of marker k with respect to camera l
$Q_b \in \mathbb{R}$	=	rigid-body angular velocity (y axis)
$\hat{Q}_b \in \mathbb{R}$	=	rigid-body rate gyro output (y axis)
$Q_j \in \mathbb{R}$	=	jth station angular velocity (y axis)
$\hat{Q}_j \in \mathbb{R}$	=	jth rate gyro output (y axis)
$R_b \in \mathbb{R}$	=	rigid-body angular velocity (z axis)
$\hat{R}_b \in \mathbb{R}$	=	rigid-body rate gyro output (z axis)
$R_j \in \mathbb{R}$	=	jth station angular velocity (z axis)
$\hat{R}_j \in \mathbb{R}$	=	jth rate gyro output (z axis)
$\boldsymbol{r} \in \mathbb{R}^3$	=	displacement vector
$\boldsymbol{r}_f \in \mathbb{R}^3$	=	displacement vector in body frame
$s \in \mathbb{R}_+$	=	wing arc length
$s' \in \mathbb{R}_+$	=	arbitrary wing arc length
$s_j \in \mathbb{R}_+$	=	arc length of jth rate gyro
$t \in \mathbb{R}$	=	time instant
$\boldsymbol{w}_j^{(g)} \in \mathbb{R}^3$	=	jth rate gyro noise
$\boldsymbol{x}_{\text{EKF}} \in \mathbb{R}^{3N+3M}$	=	extended Kalman filter state
$\hat{\boldsymbol{x}}(s) \in \mathbb{R}^3$	=	local wing x axis
$\hat{\boldsymbol{x}}_b \in \mathbb{R}^3$	=	body x axis
$\hat{\boldsymbol{y}}(s) \in \mathbb{R}^3$	=	local wing y axis
$\hat{\boldsymbol{y}}_b \in \mathbb{R}^3$	=	body y axis
$\hat{\boldsymbol{z}}(s) \in \mathbb{R}^3$	=	local wing z axis
$\hat{\boldsymbol{z}}_b \in \mathbb{R}^3$	=	body z axis
$\Gamma \in \mathbb{R}$	=	wing dihedral angle
$\delta\theta \in \mathbb{R}^N$	=	twist modal amplitudes error
$\delta\theta_i \in \mathbb{R}$	=	ith twist modal amplitude error
$\delta\phi \in \mathbb{R}^N$	=	anhedral modal amplitudes error
$\delta\phi_i \in \mathbb{R}$	=	ith anhedral modal amplitude error
$\delta\psi \in \mathbb{R}^N$	=	sweep modal amplitudes error
$\delta\psi_i \in \mathbb{R}$	=	ith sweep modal amplitude error
$\boldsymbol{\varepsilon}_j \in \mathbb{R}^3$	=	jth rate gyro drift
$\Theta \in \mathbb{R}^{M\times N}$	=	modal to Euler pitch rates transformation
$\theta \in \mathbb{R}$	=	local twist angle
$\boldsymbol{\theta} \in \mathbb{R}^N$	=	twist modal amplitudes
$\theta_i \in \mathbb{R}$	=	ith twist modal amplitude
$\tilde{\theta}_i \in \mathbb{R}$	=	ith twist mode shape
$\Lambda \in \mathbb{R}$	=	wing sweep angle
$\Phi \in \mathbb{R}^{M\times N}$	=	modal to Euler roll rates transformation
$\phi \in \mathbb{R}$	=	local anhedral angle
$\boldsymbol{\phi} \in \mathbb{R}^N$	=	anhedral modal amplitudes
$\varphi \in \mathbb{R}^{3N}$	=	angular to modal rates transformation
$\tilde{\phi}_i \in \mathbb{R}$	=	ith anhedral mode shape
$\phi_i \in \mathbb{R}$	=	ith anhedral modal amplitude
$\Psi \in \mathbb{R}^{M\times N}$	=	modal to Euler yaw rates transformation
$\psi \in \mathbb{R}$	=	local sweep angle
$\boldsymbol{\psi} \in \mathbb{R}^N$	=	sweep modal amplitudes
$\psi_i \in \mathbb{R}$	=	ith sweep modal amplitude
$\tilde{\psi}_i \in \mathbb{R}$	=	ith sweep mode shape
$\boldsymbol{\omega}_b \in \mathbb{R}^3$	=	rigid-body ground truth velocity
$\hat{\boldsymbol{\omega}}_b \in \mathbb{R}^3$	=	rigid-body rate gyro output
$\boldsymbol{\omega}_j \in \mathbb{R}^3$	=	jth station ground truth velocity
$\hat{\boldsymbol{\omega}}_j \in \mathbb{R}^3$	=	jth rate gyro output

*Post-Doctoral Research Fellow, Department of Aerospace Engineering.
†Professor, Department of Aerospace Engineering.
‡Clarence L. "Kelly" Johnson Professor, Department of Aerospace Engineering.
§Loads and Aeroelastics Engineer.

I. Introduction

THE resulting increased structural flexibility in high-aspect-ratio wing designs progressively couples aeroelastics with flight dynamics and generally gives rise to instability and/or poor handling qualities. Stable and safe piloting calls for stability augmentation systems (SASs) that simultaneously account for elastic and traditional flight dynamics degrees of freedom. Consequently, in-flight estimation of wing shape is beneficial for the control of very flexible aircraft (VFA). This paper presents a novel technique for wing shape estimation in the presence of large wing deflections based on approaches from the field of inertial navigation.

A state estimator is herein called a *flight dynamics model-based estimator* if its design requires a mathematical dynamic model of the aircraft relating actuator values (e.g., ailerons deflection, flap configuration) to system state trajectory (e.g., velocity, attitude, structural modal amplitudes). Such estimators are vehicle dependent, and their application to modified aircraft designs entails lengthy re-identification/tuning campaigns, e.g., wind tunnel testing, numerical simulations, and flight testing. Additionally, even when a model is available, it is often not precise or observable enough to support state observer-based controller design. To address this challenge, this paper proposes a model-free approach to wing shape estimation using inertial sensors. The technique avoids strain gauges and fiber Bragg gratings (FBG) [1] sensing due to their structural strain–displacement modeling requirements, although their use as complementary aiding sensors is still feasible.

An alternative flight dynamics model-free approach is to employ sighting devices and stereo-vision tracking of visual references on the wing. Whereas by using existing rivets or joint lines (natural candidates for markers) Tagai et al. [2] failed to achieve satisfactory estimation accuracy on a Beechcraft Type 65 Queen Air, experiments with artificial markers yielded subpixel precision. Alternatively, Meyer et al. [3] employed the image pattern correlation technique (IPCT) to exploit surfaces covered with random patterns (i.e., texture) to estimate wing, slat, and flap deformations on an Airbus A320. Rudnik and Schwetzler [4] exploited the same experimental apparatus to study low-speed high lift and significantly enhance the accuracy and reliability of the prediction of maximum lift for commercial aircraft.

Similarly, Kirmse [5] employed IPCT to estimate the wing shape of a VUT100 Cobra airplane. During the flight, aircraft vibration caused significant camera misalignment that ground vibration tests failed to reproduce. To correct for misalignment during postflight analysis, Kirmse [5] proposed a technique for recalibration of extrinsic parameters (e.g., camera position and orientation) based on visual data. Camera misalignment also posed a challenge in Ref. [6] in the study of a high-altitude long-endurance vehicle. In the latter, intrinsic parameters remained practically constant during flight.

In computer vision, outdoor lighting poses additional problems. In fact, Kurita et al. [7] devised the flight plan for experiments to optimize lighting conditions to study static load deformations on a Cessna Citation Sovereign. Interestingly, because the cameras were installed inside the cabin, the intrinsic optical parameters were a function of cabin pressure due to window displacement (and therefore compound lens reconfiguration) caused by fuselage deformation. Pang et al. [8] additionally warn of difficulties due to optimal shutter speed values being dependent on lighting conditions, and light reflection from the wing, which was significantly reduced by application of a light dusting of nonreflective flat white paint for accurate optical tracking of high-intensity light-emitting diodes (LEDs). A similar approach using LEDs and videogrammetry was previously developed for the measurement of wing twist and deflection as a function of time of an F/A-18 research aircraft at NASA's Dryden Flight Research Center [9]. However, the LED housings, especially outboard toward the trailing edge of the wing, were barely distinguishable from the background and called for manual selection of target image locations. Graves and Burner [10] used retro-reflective tape targets to ensure high-contrast imagery. This allowed for automated target detection employing blob analysis. Liu et al. [11] provide a comprehensive and systematic summary of photogrammetric techniques for aerospace applications.

All computer vision algorithms mentioned above are run offline after flight testing. A different approach in Ref. [12] pursued in-flight estimation from active LED markers detection by analog electro-optic receivers and allowed for continuous data sampling and processing. However, accurate calibration of analog systems is challenging and prone to noise; thus, engineering practice usually favors digital systems. Nevertheless, after an extensive and complex calibration procedure, this system successfully provided real-time continuous-time data for a 0.44-scale model of a 17,000-lb fighter airplane.

In-flight wing shape estimators for use in SASs must satisfy hard real-time computation constraints and high-bandwidth requirements, thus prohibiting employment of standalone computer vision systems. A practical alternative often pursued in navigation systems is to resort to inertial sensors for high-bandwidth data while exploiting low-bandwidth aiding sensors (e.g., global navigation satellite system receivers, cameras) for bounding divergent estimation errors. In Refs. [13,14], extended Kalman filters (EKFs) were implemented, which combined data from flight dynamics models and inertial sensors to obtain accurate results for bending; unfortunately, in Ref. [13] the estimator failed to characterize twist satisfactorily. Additionally, the techniques in Refs. [13,14] rely on an EKF formulation that precludes simple tuning due to lack of information on the statistics of the flight dynamics modeling errors. Finally, the approach in Ref. [13] assumed small wing deflections, thus hindering its application to VFA.

To the best of the authors' knowledge, this paper is the first attempt to use the aided inertial navigation framework to estimate wing shape without resorting to flight dynamics models, and its main contribution is a novel extended Kalman filter-based technique for wing shape estimation based on distributed rate gyros and optional auxiliary sensors. Because of the use of Kalman filtering, there is great flexibility in the choice of aiding sensors type, precision, sampling rates, and number. Herein a case study with sighting devices illustrates the technique and its properties. The resulting real-time estimator 1) does not require a flight dynamics model of the aircraft, 2) has a straightforward tuning procedure, 3) has an adequate bandwidth for VFA control purposes, and 4) allows for large and nonlinear wing deflections.

The remainder of the paper is organized as follows: Sec. II proposes a standalone rate gyro algorithm for wing shape estimation, and Sec. III illustrates the proposed formulation of an extended Kalman filter to incorporate additional sensor data and enhance estimation precision. Section IV illustrates the approach using cameras as aiding devices. Section V investigates the sensor placement impact on filter observability, and Sec. VI summarizes the main findings of the paper.

II. Standalone Rate Gyro Wing Shape Estimation

A. Algorithm Derivation

This section introduces a technique for estimating wing shape using an array of rate gyros. Consider an aircraft equipped with M rate gyros distributed along its right wing (see Fig. 1). Consider additionally, the aircraft inertial navigation system (INS) and, accordingly, its associated global aircraft frame $\{\hat{x}_b, \hat{y}_b, \hat{z}_b\}$. The global aircraft frame will be considered as the rigid-body reference to which flexible frames will be defined. The structural deflection is modeled by defining a deformation reference line (DRL) fixed to the wing structure (see Fig. 1). Furthermore, the DRL is defined such that it contains all M rate gyros. The DRL shape is parameterized by Euler angle functions $\phi(s, t)$, $\theta(s, t)$, and $\psi(s, t)$, where $s \in \mathbb{R}^+$ denotes the arc length along the reference line ($s = 0$ at the wing root). In this work, the angles $\phi(s, t)$, $\theta(s, t)$, and $\psi(s, t)$ are called local anhedral, local twist, and local sweep angles, respectively, and they model the orientation of the local wing frame $\{\hat{x}(s), \hat{y}(s), \hat{z}(s)\}$ with respect to the body-fixed global aircraft frame $\{\hat{x}_b, \hat{y}_b, \hat{z}_b\}$. This formulation is similar to the Frenet–Serret trajectory-based frames approach [15] and neglects extension effects. Therefore, to increase method accuracy, the DRL should be located as close as possible to the wing neutral axis, i.e., the axis along which there are no longitudinal stresses or strains.

Figure 2 further illustrates the proposed deformation description and axes conventions. If all three local angles are zero at $s = s'$, i.e.,
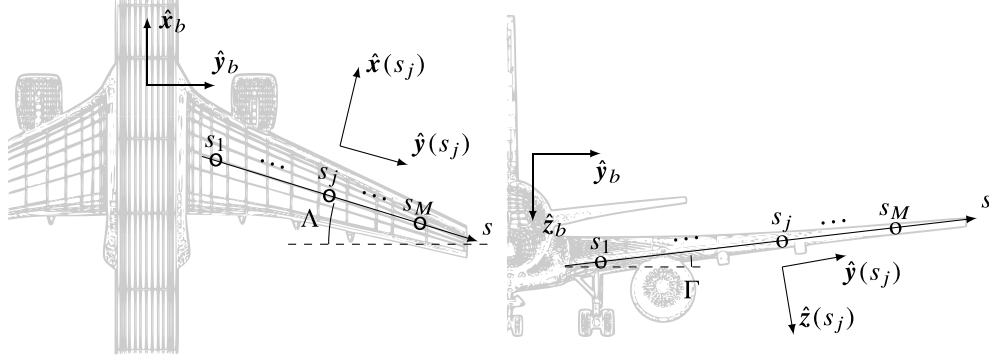
Fig. 1 Rate gyros placement and deformation reference line *s* definition.
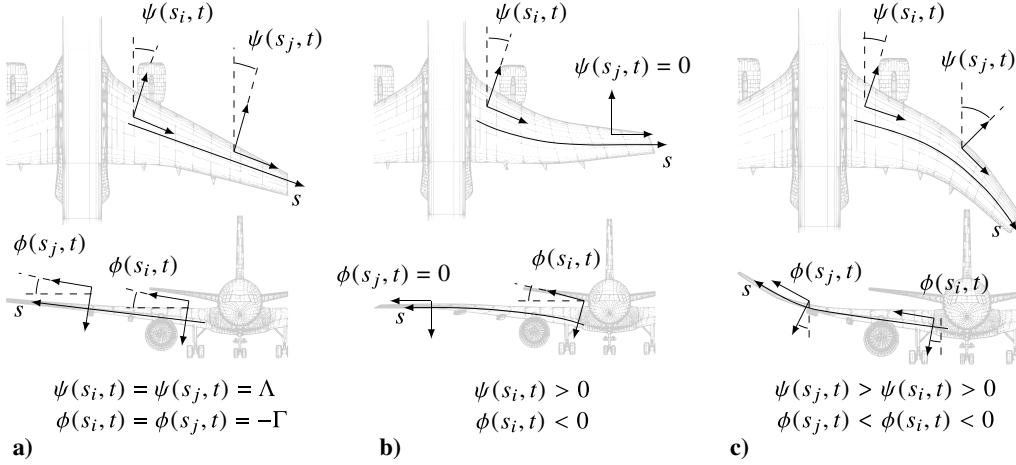

Fig. 2 Deformation examples.

$\phi(s', t) = \theta(s', t) = \psi(s', t) = 0$, then the wing section axes at $s = s'$ align with the aircraft body axes, as Fig. 2b suggests. Therefore, zero local angles do not necessarily correspond to undeformed wing shape. Additionally, spatially constant angle functions model sweep and dihedral angles (Λ and Γ, respectively), as Fig. 2a suggests. This paper defines the DRL as always tangent to the local $\hat{y}(s)$. Figures 2b and 2c illustrate orientation and right-handed sign conventions where the $\hat{z}$ (ψ)–$\hat{y}$ (θ)–$\hat{x}$ (ϕ) rotation order is assumed from body to the local wing section. This rotation order introduces a singularity in $\theta = 90°$, which is unlikely to happen even in VFA. On the other hand, an alternative rotation order such as $\hat{z}$ (ψ)–$\hat{x}$ (ϕ)–$\hat{y}$ (θ) introduces a singularity in $\phi = 90°$, which may occur in VFA.

The jth rate gyro is installed at $s = s_j$, and it is considered aligned with $\{\hat{x}(s_j), \hat{y}(s_j), \hat{z}(s_j)\}$ without loss of generality. The corresponding angle functions are described as a superposition of N basis modes, i.e.,

$$\phi(s_j, t) = \sum_{i=1}^{N} \tilde{\phi}_i(s_j)\phi_i(t) \quad \text{for } j = 1, \ldots, M \tag{1}$$

$$\theta(s_j, t) = \sum_{i=1}^{N} \tilde{\theta}_i(s_j)\theta_i(t) \quad \text{for } j = 1, \ldots, M \tag{2}$$

$$\psi(s_j, t) = \sum_{i=1}^{N} \tilde{\psi}_i(s_j)\psi_i(t) \quad \text{for } j = 1, \ldots, M \tag{3}$$

where the symbols ϕ, $\tilde{\phi}_i$, and ϕ_i denote deformation angle, mode shapes, and modal amplitudes, respectively. Furthermore, a column vector of modal amplitudes is denoted by a bold symbol, e.g., $\boldsymbol{\phi} = (\phi_1, \ldots, \phi_N)^T$. The basis modes $\{\tilde{\phi}_i, \tilde{\theta}_i, \tilde{\psi}_i : i = 1, \ldots, N\}$; are chosen to minimize N by accounting for most recurrent shapes occurring during flight, for instance, by proper orthogonal decomposition of finite element method simulations to varying loads or eigenmodes of a representative mass condition [16].

The jth rate gyro yields angular velocity measurements such that

$$\begin{pmatrix} \hat{P}_j \\ \hat{Q}_j \\ \hat{R}_j \end{pmatrix} = \begin{pmatrix} P_j \\ Q_j \\ R_j \end{pmatrix} + \boldsymbol{\varepsilon}_j + \boldsymbol{w}_j^{(g)} \tag{4}$$

where $\boldsymbol{\varepsilon}_j$ and $\boldsymbol{w}_j^{(g)}$ are, respectively, jth rate gyro's drift and noise. Additionally, $\boldsymbol{\omega}_j = (P_j, Q_j, R_j)^T$ and $\hat{\boldsymbol{\omega}}_j = (\hat{P}_j, \hat{Q}_j, \hat{R}_j)^T$ denote ground truth and measured angular velocities described in the jth rate gyro local frame $\{\hat{x}(s), \hat{y}(s), \hat{z}(s)\}$, respectively. Similarly, $\boldsymbol{\omega}_b = (P_b, Q_b, R_b)^T$ and $\hat{\boldsymbol{\omega}}_b = (\hat{P}_b, \hat{Q}_b, \hat{R}_b)^T$ denote ground truth and measured angular velocities expressed in the global rate gyro frame $\{\hat{x}_b, \hat{y}_b, \hat{z}_b\}$, respectively. Angular velocities are related to the derivatives of the Euler angles according to

$$\frac{\partial}{\partial t} \begin{pmatrix} \phi(s_j, t) \\ \theta(s_j, t) \\ \psi(s_j, t) \end{pmatrix}$$

$$= \underbrace{\begin{bmatrix} 1 & \sin\phi(s_j, t)\tan\theta(s_j, t) & \cos\phi(s_j, t)\tan\theta(s_j, t) \\ 0 & \cos\phi(s_j, t) & -\sin\phi(s_j, t) \\ 0 & \frac{\sin\phi(s_j, t)}{\cos\theta(s_j, t)} & \frac{\cos\phi(s_j, t)}{\cos\theta(s_j, t)} \end{bmatrix}}_{H(\phi(s_j, t), \theta(s_j, t), \psi(s_j, t))}$$

$$\times \begin{pmatrix} P_j(t) - D_j^b(t)P_b(t) \\ Q_j(t) - D_j^b(t)Q_b(t) \\ R_j(t) - D_j^b(t)R_b(t) \end{pmatrix} \tag{5}$$

where $D_j^b(t)$ is the direction cosine matrix from $\{\hat{\boldsymbol{x}}_b(t), \hat{\boldsymbol{y}}_b(t), \hat{\boldsymbol{z}}_b(t)\}$ to $\{\hat{\boldsymbol{x}}(s_j, t), \hat{\boldsymbol{y}}(s_j, t), \hat{\boldsymbol{z}}(s_j, t)\}$, given by

$$D_j^b(t) = \begin{bmatrix} \cos\theta\cos\psi & \cos\theta\sin\psi & -\sin\theta \\ (-\cos\phi\sin\psi + \sin\phi\sin\theta\cos\psi) & (\cos\phi\cos\psi + \sin\phi\sin\theta\sin\psi) & \sin\phi\cos\theta \\ (\sin\phi\sin\psi + \cos\phi\sin\theta\cos\psi) & (-\sin\phi\cos\psi + \cos\phi\sin\theta\sin\psi) & \cos\phi\cos\theta \end{bmatrix} \tag{6}$$

and $\phi = \phi(s_j, t)$, $\theta = \theta(s_j, t)$ and $\psi = \psi(s_j, t)$, as a shorthand notation.

The first, second, and third rows of H are denoted by $\boldsymbol{H}_\phi^T$, $\boldsymbol{H}_\theta^T$, and $\boldsymbol{H}_\psi^T$, respectively, such that

$$\boldsymbol{H}_\phi\Big(\phi(s_j, t), \theta(s_j, t), \psi(s_j, t)\Big)$$
$$= \begin{bmatrix} 1 & \sin\phi(s_j, t)\tan\theta(s_j, t) & \cos\phi(s_j, t)\tan\theta(s_j, t) \end{bmatrix}^T \tag{7}$$

$$\boldsymbol{H}_\theta\Big(\phi(s_j, t), \theta(s_j, t), \psi(s_j, t)\Big) = \begin{bmatrix} 0 & \cos\phi(s_j, t) & -\sin\phi(s_j, t) \end{bmatrix}^T \tag{8}$$

$$\boldsymbol{H}_\psi\Big(\phi(s_j, t), \theta(s_j, t), \psi(s_j, t)\Big) = \begin{bmatrix} 0 & \frac{\sin\phi(s_j,t)}{\cos\theta(s_j,t)} & \frac{\cos\phi(s_j,t)}{\cos\theta(s_j,t)} \end{bmatrix}^T \tag{9}$$

To avoid clutter, the compound function notation $\boldsymbol{H}_\phi(s_j, t)$, $\boldsymbol{H}_\theta(s_j, t)$, and $\boldsymbol{H}_\psi(s_j, t)$ will be used for the left-hand sides of Eqs. (7–9). Furthermore, note that

$$\frac{\partial}{\partial t}\phi(s_j, t) = \sum_{i=1}^{N} \tilde{\phi}_i(s_j)\dot{\phi}_i(t) \qquad \text{for } j = 1, \ldots, M \tag{10}$$

$$\frac{\partial}{\partial t}\theta(s_j, t) = \sum_{i=1}^{N} \tilde{\theta}_i(s_j)\dot{\theta}_i(t) \qquad \text{for } j = 1, \ldots, M \tag{11}$$

$$\frac{\partial}{\partial t}\psi(s_j, t) = \sum_{i=1}^{N} \tilde{\psi}_i(s_j)\dot{\psi}_i(t) \qquad \text{for } j = 1, \ldots, M \tag{12}$$

and thus, using Eq. (5) and the definition of $\boldsymbol{\omega}_j$, one obtains

$$\boldsymbol{H}_\phi^T(\boldsymbol{\omega}_j - D_j^b\boldsymbol{\omega}_b) = \sum_{i=1}^{N} \tilde{\phi}_i(s_j)\dot{\phi}_i(t) \qquad \text{for } j = 1, \ldots, M \tag{13}$$

$$\boldsymbol{H}_\theta^T(\boldsymbol{\omega}_j - D_j^b\boldsymbol{\omega}_b) = \sum_{i=1}^{N} \tilde{\theta}_i(s_j)\dot{\theta}_i(t) \qquad \text{for } j = 1, \ldots, M \tag{14}$$

$$\boldsymbol{H}_\psi^T(\boldsymbol{\omega}_j - D_j^b\boldsymbol{\omega}_b) = \sum_{i=1}^{N} \tilde{\psi}_i(s_j)\dot{\psi}_i(t) \qquad \text{for } j = 1, \ldots, M \tag{15}$$

which can be recast as the following systems of linear algebraic equations:

$$\begin{pmatrix} \boldsymbol{H}_\phi^T(s_1, t)(\boldsymbol{\omega}_1 - D_j^b\boldsymbol{\omega}_b) \\ \vdots \\ \boldsymbol{H}_\phi^T(s_M, t)(\boldsymbol{\omega}_M - D_j^b\boldsymbol{\omega}_b) \end{pmatrix} = \underbrace{\begin{bmatrix} \tilde{\phi}_1(s_1) & \cdots & \tilde{\phi}_N(s_1) \\ \vdots & \ddots & \vdots \\ \tilde{\phi}_1(s_M) & \cdots & \tilde{\phi}_N(s_M) \end{bmatrix}}_{\Phi} \begin{pmatrix} \dot{\phi}_1 \\ \vdots \\ \dot{\phi}_N \end{pmatrix} \tag{16}$$

$$\begin{pmatrix} \boldsymbol{H}_\theta^T(s_1, t)(\boldsymbol{\omega}_1 - D_j^b\boldsymbol{\omega}_b) \\ \vdots \\ \boldsymbol{H}_\theta^T(s_M, t)(\boldsymbol{\omega}_M - D_j^b\boldsymbol{\omega}_b) \end{pmatrix} = \underbrace{\begin{bmatrix} \tilde{\theta}_1(s_1) & \cdots & \tilde{\theta}_N(s_1) \\ \vdots & \ddots & \vdots \\ \tilde{\theta}_1(s_M) & \cdots & \tilde{\theta}_N(s_M) \end{bmatrix}}_{\Theta} \begin{pmatrix} \dot{\theta}_1 \\ \vdots \\ \dot{\theta}_N \end{pmatrix} \tag{17}$$

$$\begin{pmatrix} \boldsymbol{H}_\psi^T(s_1, t)(\boldsymbol{\omega}_1 - D_j^b\boldsymbol{\omega}_b) \\ \vdots \\ \boldsymbol{H}_\psi^T(s_M, t)(\boldsymbol{\omega}_M - D_j^b\boldsymbol{\omega}_b) \end{pmatrix} = \underbrace{\begin{bmatrix} \tilde{\psi}_1(s_1) & \cdots & \tilde{\psi}_N(s_1) \\ \vdots & \ddots & \vdots \\ \tilde{\psi}_1(s_M) & \cdots & \tilde{\psi}_N(s_M) \end{bmatrix}}_{\Psi} \begin{pmatrix} \dot{\psi}_1 \\ \vdots \\ \dot{\psi}_N \end{pmatrix} \tag{18}$$

Note that Φ, Θ, and Ψ depend only on the choice of basis functions and sensor placement. Assuming $M > N$ and invertibility of $\Phi^T\Phi$, $\Theta^T\Theta$, and $\Psi^T\Psi$, the least-squares solutions of Eqs. (16–18) are given by

$$\begin{pmatrix} \dot{\phi}_1 \\ \vdots \\ \dot{\phi}_N \end{pmatrix} = (\Phi^T\Phi)^{-1}\Phi^T \begin{pmatrix} \boldsymbol{H}_\phi^T(s_1, t)(\boldsymbol{\omega}_1 - D_j^b\boldsymbol{\omega}_b) \\ \vdots \\ \boldsymbol{H}_\phi^T(s_M, t)(\boldsymbol{\omega}_M - D_j^b\boldsymbol{\omega}_b) \end{pmatrix} \tag{19}$$

$$\begin{pmatrix} \dot{\theta}_1 \\ \vdots \\ \dot{\theta}_N \end{pmatrix} = (\Theta^T\Theta)^{-1}\Theta^T \begin{pmatrix} \boldsymbol{H}_\theta^T(s_1, t)(\boldsymbol{\omega}_1 - D_j^b\boldsymbol{\omega}_b) \\ \vdots \\ \boldsymbol{H}_\theta^T(s_M, t)(\boldsymbol{\omega}_M - D_j^b\boldsymbol{\omega}_b) \end{pmatrix} \tag{20}$$

$$\begin{pmatrix} \dot{\psi}_1 \\ \vdots \\ \dot{\psi}_N \end{pmatrix} = (\Psi^T\Psi)^{-1}\Psi^T \begin{pmatrix} \boldsymbol{H}_\psi^T(s_1, t)(\boldsymbol{\omega}_1 - D_j^b\boldsymbol{\omega}_b) \\ \vdots \\ \boldsymbol{H}_\psi^T(s_M, t)(\boldsymbol{\omega}_M - D_j^b\boldsymbol{\omega}_b) \end{pmatrix} \tag{21}$$

Integrating Eqs. (19–21) in time yields the standalone rate gyro wing shape estimation (RG-WSE) algorithm. All estimated outputs from the RG-WSE algorithm are represented in this work with a hat on its corresponding symbol. For instance, $\hat{\phi}_1(t)$ is the RG-WSE estimate of $\phi_1(t)$. Additionally, in state-space representation, Eqs. (19–21) can be recast as $\dot{\boldsymbol{x}} = \varphi(\boldsymbol{x}, \boldsymbol{u})$, where $\boldsymbol{x} = (\boldsymbol{\phi}, \boldsymbol{\theta}, \boldsymbol{\psi})$ and $\boldsymbol{u} = (\boldsymbol{\omega}_1, \ldots, \boldsymbol{\omega}_M, \boldsymbol{\omega}_b)$. Figure 3 illustrates the algorithm's input and output variables. Inputs are angular velocity measurements at M multiple wing locations and at the global aircraft frame, and outputs are modal amplitudes in a truncated N-dimensional space of deformation modes, i.e., $\hat{\boldsymbol{\phi}}, \hat{\boldsymbol{\theta}}$, and $\hat{\boldsymbol{\psi}} \in \mathbb{R}^N$.
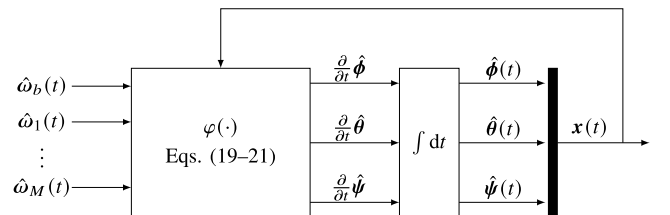

Fig. 3 Schematic of RG-WSE algorithm.

B. RG-WSE Angles to Displacement Formulation Transformation

Although the RG-WSE algorithm uses an angle-based parameterization of wing deformation, displacement-based coordinates are often desired instead. This section presents how to transform between these descriptions.

Figure 4 illustrates both descriptions at the same point $s = s_j$. At any given time t, the displacement formulation $\boldsymbol{r}(s, t)$ maps a given point s units of distance away from the wing root along the wing shape. At a fixed instant of time t, note that

$$\frac{\partial \boldsymbol{r}}{\partial s}(s, t) = \hat{\boldsymbol{y}}(s, t) \tag{22}$$

since $\boldsymbol{r}(s, t)$ is parameterized by the arc length. In the body-fixed frame $\{\hat{\boldsymbol{x}}_b, \hat{\boldsymbol{y}}_b, \hat{\boldsymbol{z}}_b\}$, integrating Eq. (22) yields

$$\boldsymbol{r}_f(s, t) = \int_0^s D(\phi(s, t), \theta(s, t), \psi(s, t))^T (0 \quad 1 \quad 0)^T \, \mathrm{d}s \tag{23}$$

where $\boldsymbol{r}_f$ is the displacement vector described in the body frame, and $D(\phi, \theta, \psi)$ is the direction cosine matrix given by

$$D(\phi, \theta, \psi) = \begin{bmatrix} \cos\theta\cos\psi & \cos\theta\sin\psi & -\sin\theta \\ (-\cos\phi\sin\psi + \sin\phi\sin\theta\cos\psi) & (\cos\phi\cos\psi + \sin\phi\sin\theta\sin\psi) & \sin\phi\cos\theta \\ (\sin\phi\sin\psi + \cos\phi\sin\theta\cos\psi) & (-\sin\phi\cos\psi + \cos\phi\sin\theta\sin\psi) & \cos\phi\cos\theta \end{bmatrix} \tag{24}$$

where $\phi(s, t)$, $\theta(s, t)$, and $\psi(s, t)$ are obtained according to Sec. II.A.

C. RG-WSE-Based Wing Coordinates

In previous sections, the wing deformation was kinetically described as an elastica with torsion and two bending degrees of freedom related to the local angles attached to points on the wing. All rate gyros were considered installed on the DRL. However, additional sensors might be installed in stations disjoint from the DRL. In this case, an extrapolation model for positioning points not belonging to the deformation line is required.

Each point on the wing can be described by the sum of a reference point $\boldsymbol{r}_f(s', t)$ in the deformation line in s', and a $\Delta\boldsymbol{p}$ vector orthogonal to the DRL.

This work assumes that cross sections normal to the DRL are rigid under wing deformation. This implies that $\Delta\boldsymbol{p}$ is always written as $(\Delta x, 0, \Delta z)$ in the $\{\hat{\boldsymbol{x}}(s'), \hat{\boldsymbol{y}}(s'), \hat{\boldsymbol{z}}(s')\}$ basis, where Δx and Δz are constant in time. Therefore, every point on the wing at any given time can have its position described as the triple $(s', \Delta x, \Delta z)$; these are hereafter called wing coordinates, and relate to global frame position $\boldsymbol{p}_f$ according to

$$\boldsymbol{p}_f = \boldsymbol{r}_f(s', t) + D\big(\phi(s', t), \theta(s', t), \psi(s', t)\big)^T \begin{pmatrix} \Delta x \\ 0 \\ \Delta z \end{pmatrix} \tag{25}$$
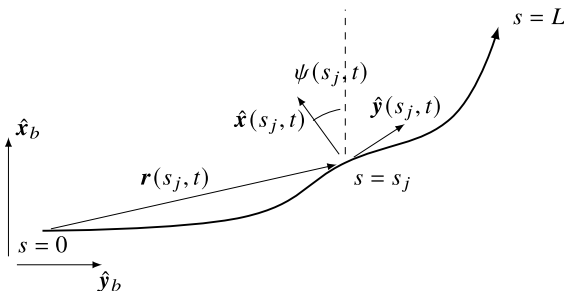

Fig. 4   Angle-based and displacement-based descriptions.

III.   RG-WSE Error Model for Extended Kalman Filtering

For fusing sensor output data with extended Kalman filtering, this work uses a linearized model for RG-WSE errors. To best conform with RG-WSE, the state vector to be estimated is composed of modal amplitude errors and rate gyro drifts. Accordingly,

$$\boldsymbol{x}_{\mathrm{EKF}} = \begin{pmatrix} \delta\phi_1 & \cdots & \delta\phi_N & \delta\theta_1 & \cdots & \delta\theta_N & \delta\psi_1 & \cdots & \delta\psi_N & \boldsymbol{\varepsilon}_1^T & \cdots & \boldsymbol{\varepsilon}_M^T & \boldsymbol{\varepsilon}_b^T \end{pmatrix}^T \tag{26}$$

where $\delta\phi_i$, $\delta\theta_i$, and $\delta\psi_i$ are defined as the difference between the ground truth and the RG-WSE-computed values. Therefore,

$$\begin{aligned} \delta\phi_i &= \phi_i - \hat{\phi}_i & \text{for } i = 1, \ldots, N \\ \delta\theta_i &= \theta_i - \hat{\theta}_i & \text{for } i = 1, \ldots, N \\ \delta\psi_i &= \psi_i - \hat{\psi}_i & \text{for } i = 1, \ldots, N \end{aligned} \tag{27}$$

or, in matrix notation, $\boldsymbol{\delta\phi} = \boldsymbol{\phi} - \hat{\boldsymbol{\phi}}$, $\boldsymbol{\delta\theta} = \boldsymbol{\theta} - \hat{\boldsymbol{\theta}}$, and $\boldsymbol{\delta\psi} = \boldsymbol{\psi} - \hat{\boldsymbol{\psi}}$. Assuming a constant rate gyro bias model (i.e., $\dot{\boldsymbol{\varepsilon}}_j = \boldsymbol{0}$), linearizing Eq. (27) with respect to the EKF state and noise yields

$$\dot{\boldsymbol{x}}_{\mathrm{EKF}} = \begin{pmatrix} \varphi(\boldsymbol{x}, \boldsymbol{u}) - \varphi(\hat{\boldsymbol{x}}, \hat{\boldsymbol{u}}) \\ \boldsymbol{0}_{3M\times 1} \end{pmatrix} \approx \underbrace{\begin{bmatrix} \frac{\partial\varphi}{\partial\boldsymbol{\phi}} & \frac{\partial\varphi}{\partial\boldsymbol{\theta}} & \frac{\partial\varphi}{\partial\boldsymbol{\psi}} & \frac{\partial\varphi}{\partial\boldsymbol{u}} \\ 0 & 0 & 0 & 0 \end{bmatrix}}_{A} \boldsymbol{x}_{\mathrm{EKF}} + \underbrace{\frac{\partial\varphi}{\partial\boldsymbol{u}}}_{G} \boldsymbol{w}^{(g)} \tag{28}$$

where $\boldsymbol{w}^{(g)}$ aggregates all the sensor noise vectors, i.e., $\boldsymbol{w}^{(g)} = (\boldsymbol{w}_1^{(g)}, \ldots, \boldsymbol{w}_M^{(g)}, \boldsymbol{w}_b^{(g)})$, and all the Jacobians are evaluated at $(\hat{\boldsymbol{x}}, \hat{\boldsymbol{u}})$, obtained here numerically by means of first-order finite differences. Similarly, a discrete-time model is obtained by

$$\begin{aligned} \boldsymbol{x}_{\mathrm{EKF}}(t_k) &\approx \boldsymbol{x}_{\mathrm{EKF}}(t_{k-1}) + \dot{\boldsymbol{x}}_{\mathrm{EKF}}\Delta t \\ &= \underbrace{(A\Delta t + I)}_{F_k} \boldsymbol{x}_{\mathrm{EKF}}(t_{k-1}) + \underbrace{G_{\mathrm{EKF}}}_{G_k} \partial\boldsymbol{w}^{(g)} \end{aligned} \tag{29}$$

where $\partial\boldsymbol{w}^{(g)}$ is the discrete-time white noise equivalent of $\boldsymbol{w}^{(g)}$. The statistics of $\partial\boldsymbol{w}^{(g)}$ should conform to rate gyro manufacturer specifications. The prediction step of the EKF is then written as

$$\begin{aligned} \hat{\boldsymbol{x}}_{k|k-1} &= F_k \hat{\boldsymbol{x}}_{k-1|k-1} \\ P_{k|k-1} &= F_k P_{k-1|k-1} F_k^T + G_k Q_k G_k^T \end{aligned} \tag{30}$$

where Q_k, $P_{k|k}$, and $P_{k|k-1}$ are the covariance of the rate gyros noise, the a posteriori error covariance matrix, and the a priori error covariance, respectively. This formulation provides a simple recipe for EKF tuning because Q_k is directly related to rate gyro manufacturer specifications. However, artificial process noise inflation might be necessary to account for linearization errors and aliasing in RG-WSE.

Figure 5 illustrates the proposed aided inertial wing shape estimator architecture. Additional aiding sensors (e.g., cameras, strain gauges, accelerometers) could be added to the architecture by means of adequate modeling of their EKF observation equations. The next section illustrates an application using sighting devices as aiding sensors. Periodical correction of RG-WSE must be performed with the acquired EKF estimates to decrease the effect of linearization
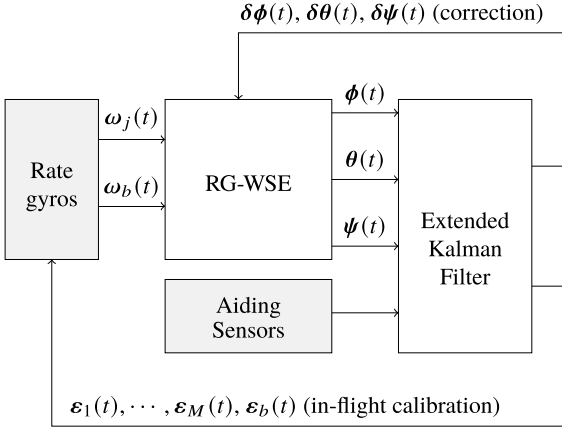
Fig. 5 Aided inertial wing shape estimator overall architecture.

errors. Additionally, the estimated rate gyro drifts are calibrated during flight by subtracting in software their biases based on Eq. (4).
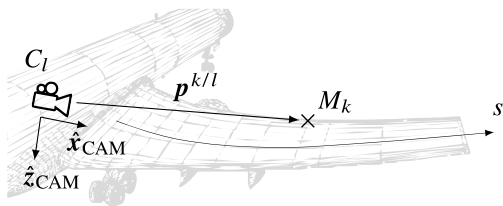
IV. Camera-Aided Rate Gyro Wing Shape Estimation

It will now be shown that integration in time of rate gyro drift and noise in Eqs. (19–21) yields unbounded RG-WSE estimation errors. Therefore, additional sensors are required to prevent estimation errors from diverging in time. Auxiliary devices can be incorporated in the RG-WSE framework by means of EKF observation equations. This work proposes an implementation of EKF update phase that employs mappings from modal amplitude errors (i.e., $\delta\phi$, $\delta\theta$, and $\delta\psi$) to auxiliary sensors output. This section illustrates this for a sighting device case study where visual markers are 1) placed at known positions on the wing, and are 2) tracked by cameras rigidly installed close to the wing root. For a given camera, the auxiliary sensor output is defined as the difference in pixels between a measured marker position and the predicted marker position based on RG-WSE outputs $\hat{\phi}$, $\hat{\theta}$, and $\hat{\psi}$, and camera–marker positioning. Multiple markers, M_k, $k = 1, \ldots, K$, tracked by multiple cameras, C_l, $l = 1, \ldots, L$, are considered.

A. EKF Observation Equations

The proposed rate gyro and sighting device data fusion technique is based on tracking visual markers M_k, each with a priori known wing location (s_k, x_k, z_k). Recall from Sec. II.C that points fixed to the wing are modeled assuming constant wing coordinates during deformation. For each marker M_k, its position with respect to a camera C_l, denoted by $p^{k/l} \in \mathbb{R}^3$, is described in the C_l camera coordinate frame using a pinhole camera model as

$$p^{k/l} = -D_l^f r_f^{C_l} + D_l^f r_f(s_k, t)$$
$$+ D_l^f D(\phi(s_k, t), \theta(s_k, t), \psi(s_k, t))^T \begin{pmatrix} x_k \\ 0 \\ z_k \end{pmatrix} \quad (31)$$

where D_l^f and $r_f^{C_l}$ denote the direction cosine matrix from body frame to camera C_l frame, and camera position with respect to wing root in body frame, respectively (see Fig. 6). All cameras are assumed fixed in body frame and thus D_k^f is constant. Hence the camera measurement $z^{k/l} \in \mathbb{R}^2$ in pixels is given by

$$z^{k/l} = \Pi \frac{f p^{k/l}}{[1 \quad 0 \quad 0] p^{k/l}} \quad (32)$$

where $f \in \mathbb{R}$ is the focal length in pixels and Π is defined by

$$\Pi = \begin{bmatrix} 0 & 1 & 0 \\ 0 & 0 & 1 \end{bmatrix} \quad (33)$$

Given these assumptions, $z^{k/l}$ depends exclusively on modal amplitudes ϕ_i, θ_i, and ψ_i, $i = 1, \ldots, N$. Therefore, $z^{k/l}$ linearization yields

$$\underbrace{z^{k/l}(\phi, \theta, \psi) - z^{k/l}(\hat{\phi}, \hat{\theta}, \hat{\psi})}_{\triangleq \Delta z^{k/l}} = \frac{\partial z^{k/l}}{\partial \phi} \delta\phi + \frac{\partial z^{k/l}}{\partial \theta} \delta\theta + \frac{\partial z^{k/l}}{\partial \psi} \delta\psi \quad (34)$$

Consequently, an appropriate model for an observation equation is given by

$$\Delta z^{k/l} = \underbrace{\left[\frac{\partial z^{k/l}}{\partial \phi} \quad \frac{\partial z^{k/l}}{\partial \theta} \quad \frac{\partial z^{k/l}}{\partial \psi} \quad \frac{\partial z^{k/l}}{\partial \varepsilon_1} \quad \cdots \quad \frac{\partial z^{k/l}}{\partial \varepsilon_M} \quad \frac{\partial z^{k/l}}{\partial \varepsilon_b} \right]}_{H^{k/l}} x_{\text{EKF}}$$
$$+ w_{\text{CAM}}^{k/l} \quad (35)$$

where $w_{\text{CAM}}^{k/l} \in \mathbb{R}^2$ is additive white Gaussian noise with statistics depending on camera quality, tracking algorithm performance, and marker–camera positioning, $(\partial z^{k/l}/\partial \varepsilon_j) = 0$ for all $j = 1, \ldots, M$, and $(\partial z^{k/l}/\partial \varepsilon_b) = 0$. With a linear sensor model in hand, the EKF incorporates measurements through the classical Kalman filter formulas [17]:

$$y_k = \Delta z^{k/l} - H^{k/l} \hat{x}_{k|k-1}$$
$$S_k = H^{k/l} P_{k|k-1}(H^{k/l})^T + R_k$$
$$K_k = P_{k|k-1}(H^{k/l})^T S_k^{-1}$$
$$\hat{x}_{k|k} = \hat{x}_{k|k-1} + K_k y_k$$
$$P_{k_k} = (I - K_k H^{k/l}) P_{k|k-1} \quad (36)$$

where $R_k = E[w_{\text{CAM}}^{k/l}(w_{\text{CAM}}^{k/l})^T]$ is the measurement noise covariance, and the mean of the measurement noise is assumed to be zero. In practice, artificial R_k inflation with respect to $w_{\text{CAM}}^{k/l}$ might be necessary to account for additional sources of uncertainties, e.g., camera vibration.

Rate gyro-based EKF prediction updates occur at a higher rate than EKF observation updates from the camera measurements. Thus
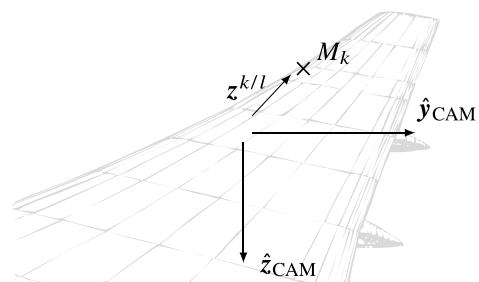
a) Camera axis definition and symbols   b) Camera view

Fig. 6 Camera-related symbols and frame definitions.

between two updates from the camera measurements per Eq. (36) there will be multiple prediction updates from the gyro measurements per Eq. (30). This allows for heterogeneous sensor configurations with respect to sampling time, and favors nonuniform sampling.

In this work, camera tracking algorithms are not considered; instead, it is assumed that image processing already took place with precision represented by $w_{\text{CAM}}^{k/l}$. Examples of target-tracking image processing algorithms in the context of wing deformation are given in Refs. [8,10]. However, Pang et al. [8] build upon a stereo vision setup to update an EKF with estimated 3D positions of markers. The present camera-aided rate gyro wing shape estimation (CRG-WSE) approach eliminates the need for stereo vision because it uses the 2D projections of markers in the camera plane directly. As a consequence, any number of cameras can be employed independently, rendering camera frame synchronization unimportant.

B. Standalone and Aided Methods Comparison

By means of computer simulation, two experiments were conducted to illustrate the degrees of observability of standalone and aided observer algorithms. In both numerical experiments, right wing shape estimation of an aircraft is pursued while performing a harmonic motion given by

$$\phi(s,t) = \Gamma + s\Gamma_0 \sin(\omega t)$$
$$\theta(s,t) = 0$$
$$\psi(s,t) = \Lambda$$
$$\omega_b(t) = \mathbf{0} \tag{37}$$

where $0 < t < t_{\text{sim}}$, $0 < s < b$. Additionally, Γ, Γ_0, Λ, and Λ_0 are scalar constants given in Table 1. The overall trajectory of the wing due to this deformation profile is illustrated in Fig. 7a. For algorithm implementation, polynomial shape basis and $N = 2$ are assumed, thus matching the number of modes in ground truth, and, accordingly,

$$\tilde{\phi}_1(s) = \tilde{\theta}_1(s) = \tilde{\psi}_1(s) = 1$$
$$\tilde{\phi}_2(s) = \tilde{\theta}_2(s) = \tilde{\psi}_2(s) = s \tag{38}$$

Table 1   Wing shape movement description in simulation

Γ	Γ_0	Λ	t_{sim}	b	ω
−0.09 rad	0.03 rad	0.36 rad	20 s	17 m	π rad/s
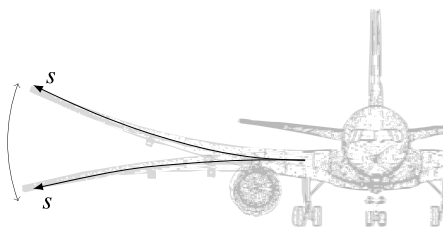
leading to ground truth values given by

$$\phi(t) = \begin{pmatrix} \phi_1(t) \\ \phi_2(t) \end{pmatrix} = \begin{pmatrix} \Gamma \\ \Gamma_0 \sin(\omega t) \end{pmatrix}, \quad \theta(t) = \begin{pmatrix} \theta_1(t) \\ \theta_2(t) \end{pmatrix} = \begin{pmatrix} 0 \\ 0 \end{pmatrix},$$
$$\psi(t) = \begin{pmatrix} \psi_1(t) \\ \psi_2(t) \end{pmatrix} = \begin{pmatrix} \Lambda \\ 0 \end{pmatrix} \tag{39}$$

Ten rate gyros were installed in the wing according to the positioning defined in Fig. 7b. In the camera-aided case, additional visual trackers and sighting devices are installed as also depicted in Fig. 7b. Their biases and noise characteristics are described in Table 2, and are purposely deteriorated with respect to the performance of low-cost inertial measurement units (IMUs) readily available in the market (e.g., the Xsens MTi 100-series) to reduce simulation time.

Figure 8 illustrates the simulation results for both standalone and camera-aided experiments. Modal amplitude and bias estimation errors are plotted with their respective 2σ EKF covariances. Moreover, $\sqrt{\delta\phi_1^2 + \delta\theta_1^2 + \delta\psi_1^2}$ and $\sqrt{\delta\phi_2^2 + \delta\theta_2^2 + \delta\psi_2^2}$ are plotted separately due to their distinct orders of magnitude.

Note that standalone estimation has its errors diverging with time; thus, its use imposes an upper bound on the duration of missions. On the other hand, the camera-aided estimator yields bounded errors. However, for the given sensor imperfection statistics, rate gyro drift is negligibly estimated because its initial covariance is only marginally greater than the steady-state filter covariance.

V.   Observability Analysis

This section studies the impact of rate gyros and visual markers number and placement on the proposed camera-aided estimator precision. For that purpose, the numerical experiment in Sec. IV.B is repeated with different sensor configurations. Since $N = 2$ was assumed, a minimum of two rate gyros is required for RG-WSE implementation, as discussed in Sec. II.A. A varying quantity from 2 to 10 rate gyros in even numbers is examined assuming equally spaced placement along the semispan b (see Fig. 9a). For each rate gyro configuration, the visual markers quantity is also varied from 2 up to 10 in even numbers. Their placement starts at the wingtip ($s = b$) and proceeds inward with 2 m spacing (see Fig. 9b). Additionally, odd- and even-numbered markers are placed toward the leading and trailing edges, respectively, but always 2 m away from the DRL.

Although a universal figure of merit for measuring observability is nonexistent [18], observability is evaluated herein through end-of-simulation EKF $P_{k|k}$ covariances comparison. In this sense, smaller
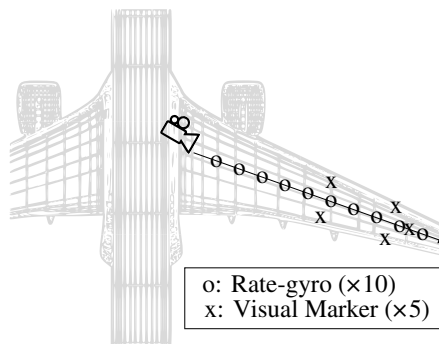
a) Deformation trajectory   b) Sensor positioning

Fig. 7   Simulation wing trajectory and sensor positioning.

Table 2   Sensor bias and noise statistics in simulation

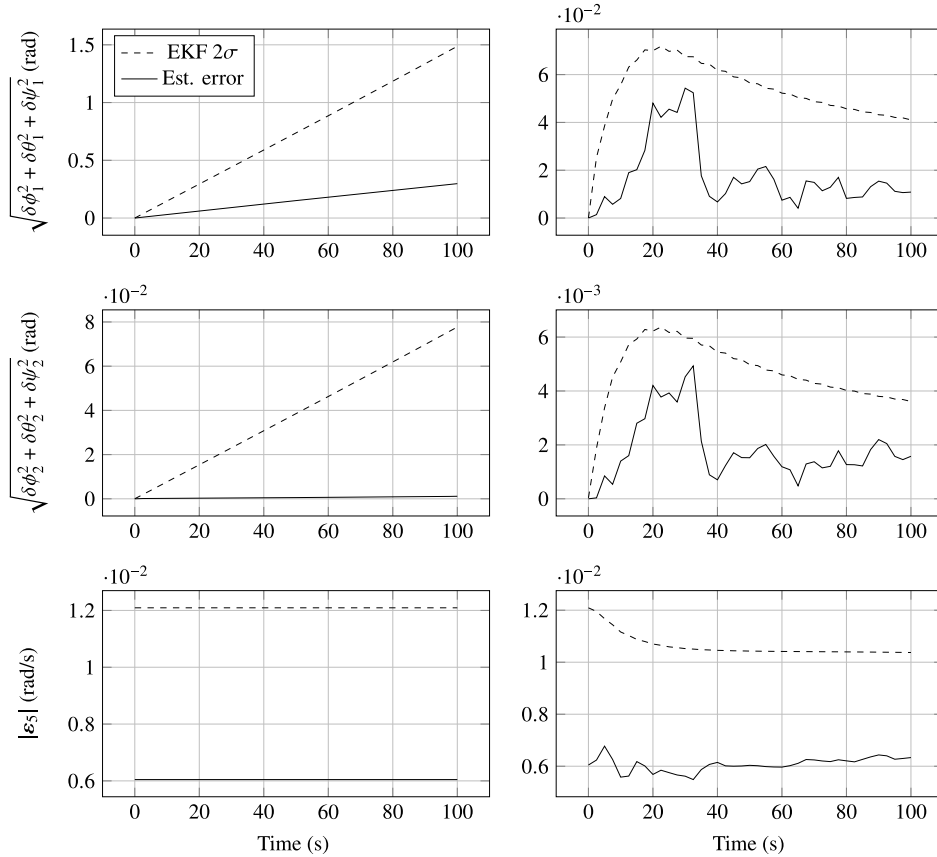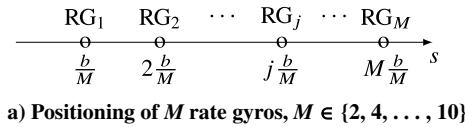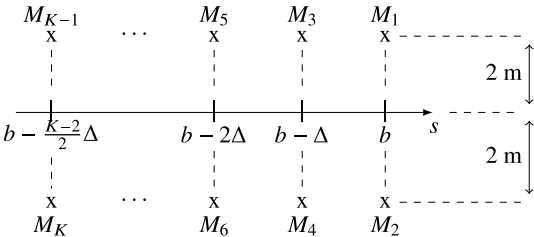| ε_b	ε_j	Rate gyro noise density ($w_j^{(g)}$)	Camera noise standard deviation ($\omega_{\text{CAM}}^{k/l}$)
$0.1 \cdot (1,1,1)$ deg/s	$0.2 \cdot (1,1,1)$ deg/s	0.01 deg/s/Hz	0.01 m (assuming $f = 1$)

Fig. 8 Comparison of estimated error and predicted EKF covariance for standalone estimation (on the left) and aided estimation (on the right).

a) Positioning of M rate gyros, $M \in \{2, 4, \ldots, 10\}$

b) Positioning of K markers, $K \in \{2, 4, \ldots, 10\}$, $\Delta = 2$ m

Fig. 9 Sensor positioning patterns for observability analysis experiments.

covariances are associated with more observable, thus more precise, configurations. Figure 10 displays end-of-simulation EKF standard deviations for each proposed configuration. Because EKF covariances vary slightly across simulation runs, due to different EKF Jacobians values occurring due to RG-WSE random errors, Fig. 10 displays the root mean square (RMS) values of Monte Carlo simulations with 10 independent runs for each configuration. Each independent simulation randomly samples different rate gyros drift ε_j and noise $w_j^{(g)}$ values. As expected, observability increases with the number of sensors and markers. However, as the number of markers increases, the impact on system accuracy of increasing the number of rate gyros gets diminished. Additionally, modal error standard deviations decrease log-linearly with the number of visual markers.

The comments above suggest some design guidelines for choosing sensor quantity numbers. First, the designer determines N by deciding how many (and which) basis modes best represent the bulk of the
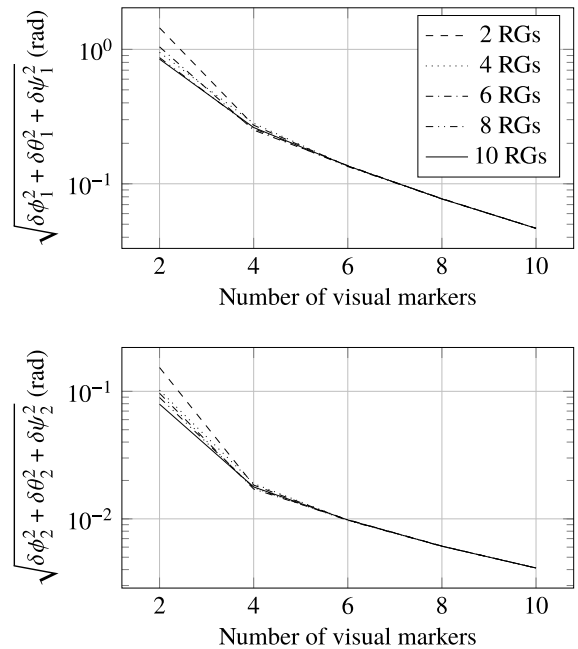

Fig. 10 EKF 2σ values at the end of the simulation ($t = 100$ s) for different instrumentation quantities.

in-flight wing deformations. The number of rate gyros M should match N, and there is little gain in adding additional units. Subsequently, the number of markers K is chosen to attain the desired performance or should be as large as the visual tracking algorithm allows without violating robustness and real-time requirements. Note that a system with no camera updates would have estimation errors diverging, whereas a system with no rate gyros would have low bandwidth as measurements are available only at camera sampling instants.
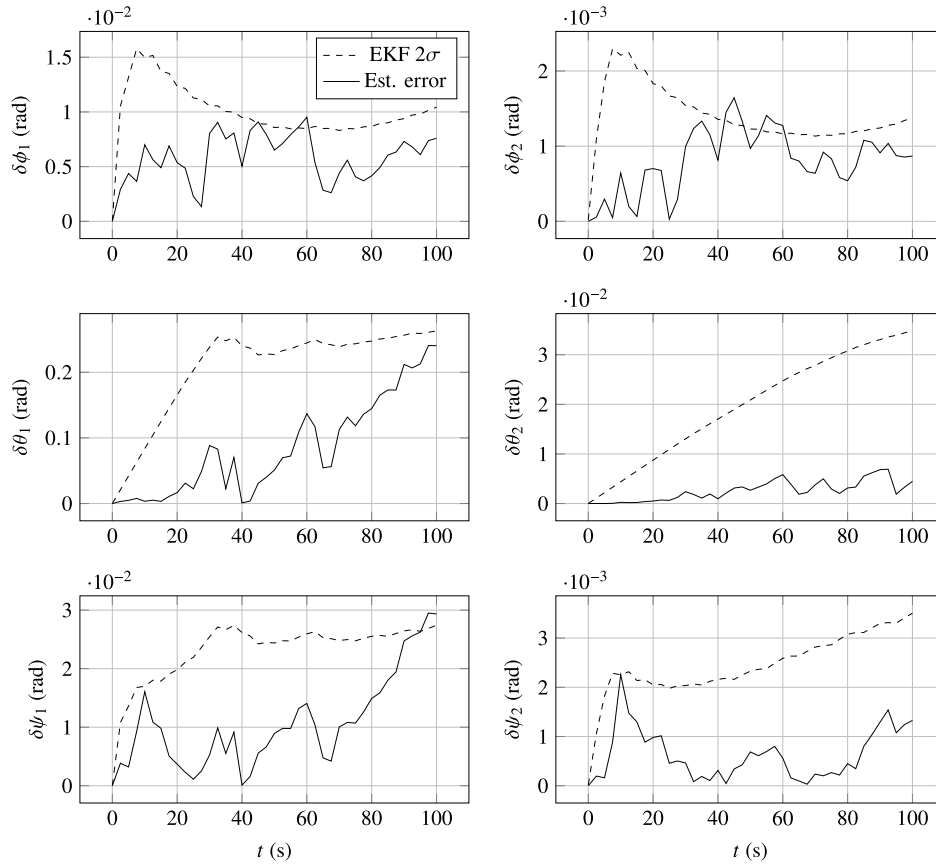
Fig. 11   Shortfall in observability of $\delta\theta_1$ and $\delta\theta_2$ due to aligned visual markers.

Although RG-WSE imposes rate gyros installation on the DRL, visual markers are allowed to be anywhere on the wing. However, some practical considerations must be respected. For example, Fig. 11 shows the outcome of a numerical experiment where five equally spaced visual markers are positioned on the reference deformation line (instead of closer to the leading and trailing edges as before). The noticeably degraded observability in $\boldsymbol{\theta}$, by a factor of 10 in precision with respect to the other components (and previous experiments in Sec. IV.B), reinforces the intuitive result that a line cannot fully define a rigid-body orientation. Therefore, rectilinear placement of markers should be avoided if wing twist estimation is pursued.

VI.   Conclusions

This paper proposed a novel technique for high-bandwidth real-time estimation of wing shape using an array of rate gyros, and lays the groundwork for tight EKF interfacing with additional sensors. Tight EKF coupling eliminates suboptimal assumptions that often reduce precision and make tuning impracticable in reality. To further facilitate tuning, the proposed technique avoids resorting to flight dynamics models because their uncertainties are difficult to characterize. Furthermore, design guidelines are provided for tuning and deciding on sensor number and placement.

The proposed technique inherits the benefits of Kalman filtering, e.g., multirate asynchronous aiding sensors integration, low computational cost, and fault detection, isolation, and recovery capabilities. In particular, this work shows that tight optical system integration yields a fully observable state estimation using a single camera. This contrasts with previous research, where loosely coupled integration called for stereo vision approaches (thus two sighting devices or more). Finally, much room remains for future research. This includes the analysis of the case when gyros are not installed on the DRL, and impact on the accuracy at higher frequencies when the camera may fail to capture all the information.

References

[1] Ma, Z., and Chen, X., "Fiber Bragg Gratings Sensors for Aircraft Wing Shape Measurement: Recent Applications and Technical Analysis," *Sensors (Basel)*, Vol. 19, No. 1, 2019, p. 55.
https://doi.org/10.3390/s19010055

[2] Tagai, R., Nakakita, K., Kurita, M., and Nakajima, T., "Wing Deformation Measurement as Bases for In-Flight Aerodynamics," *AIAA Flight Testing Conference*, AIAA Paper 2016-3355, 2016.
https://doi.org/10.2514/6.2016-3355

[3] Meyer, R., Kirmse, T., and Boden, F., "Optical In-Flight Wing Deformation Measurements with the Image Pattern Correlation Technique," *New Results in Numerical and Experimental Fluid Mechanics IX*, edited by A. Dillmann, G. Heller, E. Krämer, H. P. Kreplin, W. Nitsche, and U. Rist, Vol. 124, Notes on Numerical Fluid Mechanics and Multidisciplinary Design, Springer, Cham, Switzerland, 2014, pp. 545–553.
https://doi.org/10.1007/978-3-319-03158-3_55

[4] Rudnik, R., and Schwetzler, D., "High Lift INflight VAlidation (HINVA)—Overview About the 1st Flight Test Campaign," *32nd AIAA Applied Aerodynamics Conference*, AIAA Paper 2016-0041, 2016.
https://doi.org/10.2514/6.2016-0041

[5] Kirmse, T., "Recalibration of a Stereoscopic Camera System for In-Flight Wing Deformation Measurements," *Measurement Science and Technology*, Vol. 27, No. 5, 2016, Paper 054001.
https://doi.org/10.1088/0957-0233/27/5/054001

[6] Sanches, A. C., Silvestre, F. J., Morales, M. A. V., and Hesse, H., "Designing a Vision-Based System to Measure In-Flight Wing Deformation," *Proceedings of the 31st Congress of the International Council of the Aeronautical Sciences (ICAS)*, International Council of the Aeronautical Sciences, Bonn, 2018, pp. 1–7.

[7] Kurita, M., Koike, S., Nakakita, K., and Masui, K., "In-Flight Wing Deformation Measurement," *51st AIAA Aerospace Sciences Meeting Including the New Horizons Forum and Aerospace Exposition,*

Aerospace Sciences Meetings, AIAA Paper 2013-0967, 2013.
https://doi.org/10.2514/6.2013-967

[8] Pang, Z. Y., Cesnik, C. E. S., and Atkins, E. M., "In-Flight Wing Deformation Measurement System for Small Unmanned Aerial Vehicles," *55th AIAA/ASME/ASCE/AHS/ASC Structures, Structural Dynamics, and Materials Conference*, AIAA Paper 2014-0330, 2014.
https://doi.org/10.2514/6.2014-0330

[9] Burner, A. W., Lokos, W. A., and Barrows, D. A., "In-Flight Aeroelastic Measurement Technique Development," *Optical Diagnostics for Fluids, Solids, and Combustion II, Proceedings of SPIE*, Vol. 5191, Soc. of Photo-Optical Instrumentation Engineers, Bellingham, WA, 2003, pp. 186–199.
https://doi.org/10.1117/12.504157

[10] Graves, S. S., and Burner, A. W., "Development of an Intelligent Video-grammetric Wind Tunnel Measurement System," *Optical Diagnostics for Fluids, Solids, and Combustion, Proceedings of SPIE*, Vol. 4448, Soc. of Photo-Optical Instrumentation Engineers, Bellingham, WA, 2001, pp. 120–131.
https://doi.org/10.1117/12.449368

[11] Liu, T., Burner, A. W., Jones, T. W., and Barrows, D. A., "Photogram-metric Techniques for Aerospace Applications," *Progress in Aerospace Sciences*, Vol. 54, Oct. 2012, pp. 1–58.
https://doi.org/10.1016/j.paerosci.2012.03.002

[12] DeAngelis, V. M., "In-Flight Deflection Measurement of the HiMAT Aeroelastically Tailored Wing," *Journal of Aircraft*, Vol. 19, No. 12, 1982, pp. 1088–1094.
https://doi.org/10.2514/3.44816

[13] Kotikalpudi, A., Danowsky, B. P., Schmidt, D. K., Regan, C. D., and Gupta, A., "Real-Time Shape Estimation for a Small Flexible Flying-Wing Aircraft," *AIAA SciTech 2019 Forum*, AIAA Paper 2019-1818, 2019.
https://doi.org/10.2514/6.2019-1818

[14] Pang, Z. Y., and Cesnik, C. E. S., "Strain State Estimation of Very Flexible Unmanned Aerial Vehicle," *AIAA SciTech 2016 Forum*, AIAA Paper 2016-1955, 2016.
https://doi.org/10.2514/6.2016-1955

[15] Kreyszig, E., *Differential Geometry*, Dover, New York, 1991, pp. 40–43, Chap. 2.

[16] Medeiros, R. R., Cesnik, C. E. S., and Coetzee, E. B., "Computational Aeroelasticity Using Modal-Based Structural Nonlinear Analysis," *AIAA Journal*, Vol. 58, No. 1, 2020, pp. 362–371.
https://doi.org/10.2514/1.J058593

[17] Crassidis, J. L., and Junkins, J. L., *Optimal Estimation of Dynamic Systems*, CRC Press, Boca Raton, FL, 2011, Chap. 3.
https://doi.org/10.1201/b11154

[18] Krener, A. J., and Ide, K., "Measures of Unobservability," *Proceedings of the 48th IEEE Conference on Decision and Control*, IEEE Publ., Piscataway, NJ, 2009, pp. 6401–6406.
https://doi.org/10.1109/CDC.2009.5400067